Photoconductive Effects in Single Crystals of BaZrS₃

Boyang Zhao¹, Huandong Chen¹, Ragib Ahsan², Fei Hou³, Eric R Hoglund^{4,5,6}, Shantanu Singh¹, Maruda Shanmugasundaram⁷, Huan Zhao⁸, Andrey V. Krayev⁹, Han Htoon⁸, Patrick E Hopkins^{5,6,10}, Jan Seidel³, Rehan Kapadia², and Jayakanth Ravichandran^{1,2,11*}

¹Mork Family Department of Chemical Engineering and Materials Science, University of Southern California, Los Angeles, California, 90089, USA

²Ming Hsieh Department of Electrical Engineering, University of Southern California, Los Angeles, California, 90089, USA

³School of Materials Science and Engineering, University of New South Wales, Sydney, NSW, Australia

⁴Department of Mechanical and Aerospace Engineering, University of Virginia, Charlottesville, Virginia, 22807, USA

⁵Department of Materials Science and Engineering, University of Virginia, Charlottesville, Virginia, 22904, USA

⁶Center for Nanophase Materials Sciences, Oak Ridge National Laboratory, Oak Ridge, Tennessee 37830, USA

⁷HORIBA Instruments Inc., Piscataway NJ, 08854, USA

⁸Center for Integrated Nanotechnologies (CINT), Materials Physics and Applications Division, Los Alamos National Laboratory, Carlsbad, New Mexico, 88220, USA

⁹HORIBA Instruments Inc., Novato CA, 94949, USA

¹⁰Department of Physics, University of Virginia, Charlottesville, Virginia, 22904, USA

KEYWORDS: perovskite chalcogenide, single crystals, optoelectronics, defects, KPFM, STEM

ABSTRACT: Chalcogenide perovskites, such as BaZrS₃, are emerging semiconductors with potential for high photovoltaic power conversion efficiency. The role of defects in the efficiency of the generation and collection of photo-excited carriers has not been experimentally investigated extensively. We study the effect of processing-induced defects on the photoconductive properties of single crystals of BaZrS₃. We achieved ohmic contacts to single crystals of BaZrS₃ and observed positive surface photovoltage, which is typically observed in *p*-type semiconductors. However, mechanical polishing of BaZrS₃ to remove the surface oxide leads to dense deformation grain boundaries and leads to trap-dominated photoconductive response. In comparison, ohmic contacts achieved in cleaved crystals leave fewer deformation defects and greatly improve optoelectronic properties. Defect-controlled crystal growth and contact fabrication are potentially limiting factors for achieving high photon-to-excited electron conversion efficiency in BaZrS₃.

INTRODUCTION

From silicon, 1 GaAs, 2 to halide perovskites, 3,4 semiconductors with excellent optoelectronic properties have laid the foundation of modern photonics. Recently, a new class of inorganic semiconductors, chalcogenide perovskites,5-8 has drawn significant attention due the characteristics such as earth-abundant and non-toxic composition,9 tunable bandgap in the visible and infrared energies,5 and thermal stability.10 Polycrystalline 11,12,13,14 and epitaxial 15,16 thin films of BaZrS₃ have been used to realize prototypical metal-semiconductor heterojunctions with appreciable photoresponsivity. Solution-processed BaZrS₃ nanoparticles^{17,18,19} and thin films^{20,21,22} have been explored to realize low-cost optoelectronic devices. However, the role of extended defects i.e., grain boundaries, dislocations, and crystalline domains and interfaces during thin film growth and device fabrication has not been systematically studied yet. Hence, the intrinsic optoelectronic performance limits have not been studied, despite the availability of single crystals of Ba-ZrS₃. 23,24

In this work, we use single crystals of BaZrS₃ grown with BaCl₂ flux to establish optoelectronic device fabrication protocols. The electrical contacts to bulk BaZrS₃ crystals were fabricated after removing the oxide layers using mechanical polishing or cleavage. We studied the work function of BaZrS₃ by Kelvin Probe Microscopy (KPFM), which shows an obvious decreasing trend under optical excitation, resembling a p-type semiconductor. Conversely, two terminal ohmic electrical contacts to polished BaZrS₃ crystal show trap-dominated photo-response in time-resolved, power-dependent, or spatially mapped photocurrent measurements. The traps are presumably related to extended defects caused by mechanical deformation while polishing the surfaces. Cleaving the crystals to expose fresh surfaces to electrical contacts showed significant improvement in the optoelectronic properties, in agreement with this notion. These results show the limits posed by extended defects during materials processing for optoelectronic devices of BaZrS₃ and show the need to develop processing techniques to access the intrinsic performance limits of chalcogenide perovskite optoelectronic devices.

¹¹Core Center of Excellence in Nano Imaging, University of Southern California, Los Angeles, California, 90089, USA

RESULTS AND DISCUSSION

Crystal Growth and Contact Fabrication. Single crystals of BaZrS3 were grown in an evacuated sealed ampoule using BaCl₂ flux, as reported earlier^{21,22} (Methods I). We were able to achieve relatively larger single crystals of BaZrS₃ using the slower cooling rate (*i.e.*, cubes with sides of \sim 250 µm). First, we characterize the optoelectronic quality of the crystals using time-resolved photoluminescence (TRPL). The bi-exponential relaxation time of photo-excited states, as measured by TRPL for BaZrS₃ crystal [Figure S1] was $\tau_1 = 0.675 \pm 0.005$ ns, $\tau_2 =$ 3.97 ± 0.04 ns, shorter but comparable to the SRH recombination lifetimes (SRH) of ~50 ns 24 ($\tau_1 = 1.069 \pm 0.009$ ns, $\tau_2 =$ 8.00 ± 0.15 ns) measured on earlier BaZrS₃ crystals. We have employed a nearly O₂-free sample preparation for the flux growth,²³ and a sulfur-rich reaction condition to minimize point defects such as sulfur vacancies and oxygen substitution in sulfur during the growth, but inadvertent point defects created in the growth could have caused subtle differences in the TRPL response between these crystals.

Next, we attempted to fabricate electrical contacts to single crystals of BaZrS₃ to characterize their optoelectronic properties. As grown crystals, after extraction from the flux, invariably have a thin insulating layer of sulfate, sulfite, or oxide on the surface. Presumably, this layer is formed during exposure to water and/or air, while extracting the crystals from the salt flux, and severely limits our ability to make ohmic contacts. To overcome this issue, we resorted to mechanically polishing off (optimized by crystal embedding, details see Methods) the insulating layer [Figure 1a] or cleaving it [inset of Figure 4a] right before depositing or transferring metal contacts. Both approaches

are discussed in detail in Methods, and both achieve ohmic contacts or nearly ohmic contacts to bulk BaZrS₃.

Optoelectronic Properties. First, we leveraged stable electrical contacts to perform static surface potential measurements on BaZrS₃ using the Kelvin Probe Microscopy (KPFM)²⁵. We will use optical illumination during the KPFM studies to track the evolution of the surface potential to learn about the accumulation of the photo-excited carriers. BaZrS₃ crystals were electrically connected to AFM disks with silver paint on the backside. Contact potential difference (CPD, illustrated in Figure 1b) of BaZrS₃ is then measured [Figure S3] between the top surface [Figure 1c, Figure 1d] and the tip by KPFM, $CPD = \varphi_{tip}$ $-\varphi_{\text{BaZrS}_2}$. CPD map of BaZrS₃ and the highly oriented pyrolytic graphite (HOPG)²⁶ were measured under the same condition to calibrate the work function values determined from these measurements. BaZrS₃ work function is thus extracted to be 4.44 ± 0.02 eV (Supporting Information). This is a slightly higher work function than Ti (4.33 eV) and Ga (4.32 eV)²⁷. Both metal contacts were tested and established as ohmic contacts to Ba-ZrS3.

Next, we introduce optical illumination in the same region of KPFM to investigate the surface photovoltage (SPV) accumulation on the surface of an as-grown (Figure S3, SPV up to +0.18 V) and a polished (Figure 1a, SPV up to +0.15 V) BaZrS₃ surface. As the charge neutrality level of semiconductor surfaces bends the conduction and valence band near the free surface depending on the type of carrier in the semiconductor [Figure 1b], photo-excited carriers accumulated near the surface will dictate the band curvature, which typically leads to a positive $\Delta CPD = CPD_{\text{illuminated}} - CPD_{\text{dark}}$ in the case of p-type

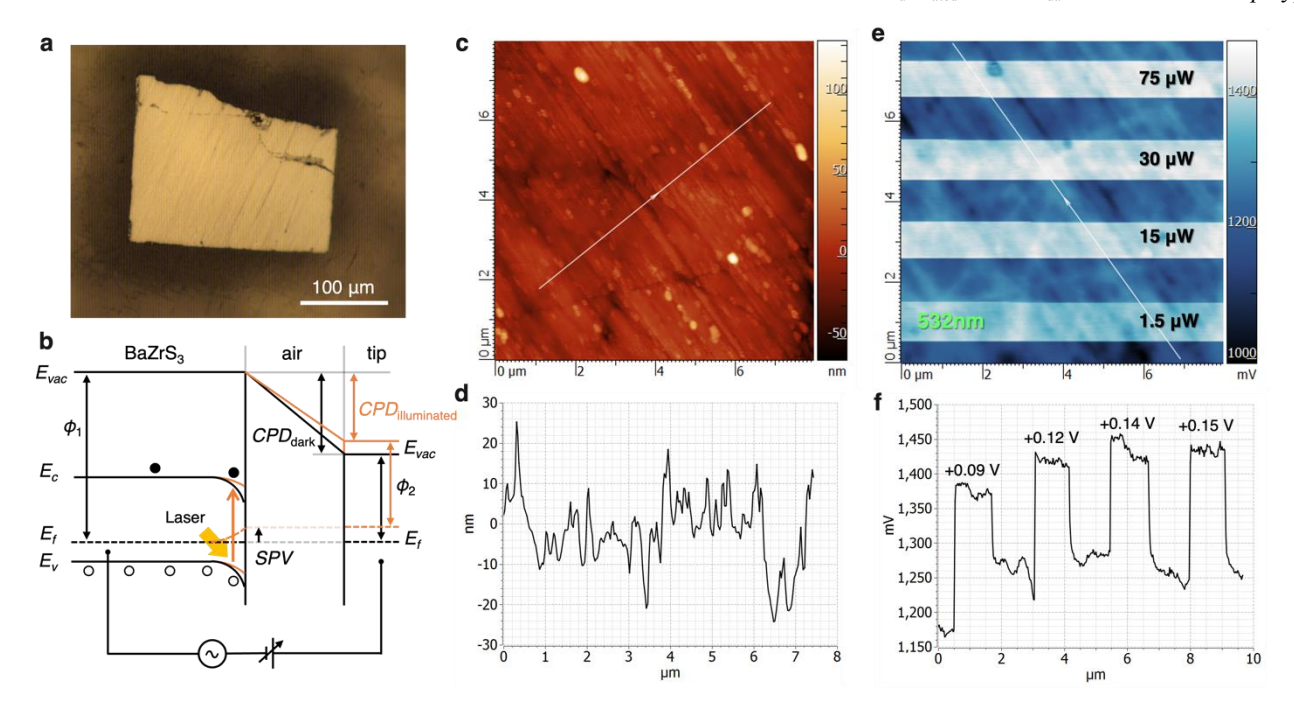


Figure 1. Surface photovoltage (SPV) characterization of BaZrS₃ *via* KPFM. (b) Illustration of the band diagram of a *p*-type semiconductor surface whose surface potential is balanced with the metallic tip of the KPFM without (black) and with (orange) illumination. (c) AFM topography of polished BaZrS₃. The surface roughness *R_a* was lower than 7 nm. (d) The spatial dependence of the topography of the polished sample corresponds to the white line noted in (c). (e) *CPD* map of the surface of BaZrS₃ crystal across the same area in (c). The optical excitation power is noted, and dark regions correspond to dark conditions without optical illumination. The *CPD* scales with optical excitation power. (f) The spatial dependence of *CPD* along the white line noted in (e).

semiconductors or negative $\triangle CPD$ in the case of *n*-type semiconductors²⁸. In BaZrS₃ [Figure S4], 785 nm excitation leads to lower $\triangle CPD$ compared to 532 nm or 638 nm excitation, as 785 nm has energy below the bandgap of BaZrS₃ $\sim 1.7-1.95$ eV^{7,16,29,30}, but a consistent positive SPV (decreasing work function) is observed, under all three excitation wavelengths. Further, the increase in SPV scales with the increase in the excitation power, which saturates beyond a certain wavelength-dependent threshold. [Figure 1e, Figure 1f]. We thus conclude that the surface photovoltage characteristics of BaZrS₃ are consistent with a p-type or a hole-mobility-dominated ambipolar semiconductor, whose acceptor level is potentially induced by Ba or Zr vacancies formed during the growth³¹. As sulfurization conditions of oxide give rise to both *n*-type¹¹ and electron-mobility-dominated ambipolar¹³ electrical transport, and colloidal BaZrS₃ achieves temperature-dependent ambipolar properties²⁰, carrier type of BaZrS₃ could be influenced to achieve both *n*- and *p*-type by doping and alloying.

Photoconductivity studies on polished crystals. Next, we fabricated two-terminal devices to study the photoconductivity response in BaZrS₃ single crystals. We made Ti/Au (details see Methods), which is nearly ohmic, and a typical device is shown in the inset of **Figure 2a**. We observed relatively linear DC current-voltage, or I-V characteristics under dark conditions, and a typical I-V curve is shown in **Figure 2a**. We observed positive photocurrent ($I - I_{dark}$, hereafter noted as photocurrent for brevity) under the illumination of 405 nm, 532 nm, and 633 nm wavelengths [**Figure 3b**], and a sharp drop in

photocurrent was observed [inset of **Figure 3c**] when we used photon energies (of 710 nm and 785 nm) below the bandgap of BaZrS₃⁷. We normalized the power density in terms of sun power (1 sun = power of AM 1.5 illumination $\sim 1000 \text{ W/m}^2$) ³² to compare the responsivity between different wavelengths of light used here. We observed a responsivity of up to $\sim 0.3 \text{ A/W}$ at 10 V under 532 nm excitation, equivalent to a ~ 0.18 external quantum efficiency (EQE). This is possibly led by either an efficient minority carrier photoexcitation or accumulated long-lifetime defect traps like BaZrS₃ thin films¹⁶.

Scanning Photocurrent Microscopy Studies. Next, we performed a scanning photocurrent microscopy (SPCM) study by scanning the focused ($\sim 0.8 \mu m$ diameter spot size, details in Supporting Information) 532 nm laser excitation across the active channel from source to drain while recording the photocurrent response to learn about the nature of the photoexcited carriers. Figure 2d shows the SPCM mapping results under different DC bias voltages. The maximum photocurrent was observed in the middle and roughly equidistant from the source and drain, irrespective of the applied voltage bias, which is inconsistent with the SPCM behavior expected from p-type nor n-type semiconductors³³ (n-type Silicon verified in Supporting Information). For degenerately doped semiconductors, we expected the maximum photocurrent to occur near the source (p-type) or drain (*n*-type) electrodes under a $+V_{\text{source}}$ ($V_{\text{drain}} = 0$), and such photocurrent profile is generally inversed under a $-V_{\text{source}}$. Past studies showed that the photo-excited minority carrier meanfree path (\sim 5 µm²⁴) for similar single crystals of BaZrS₃ is much

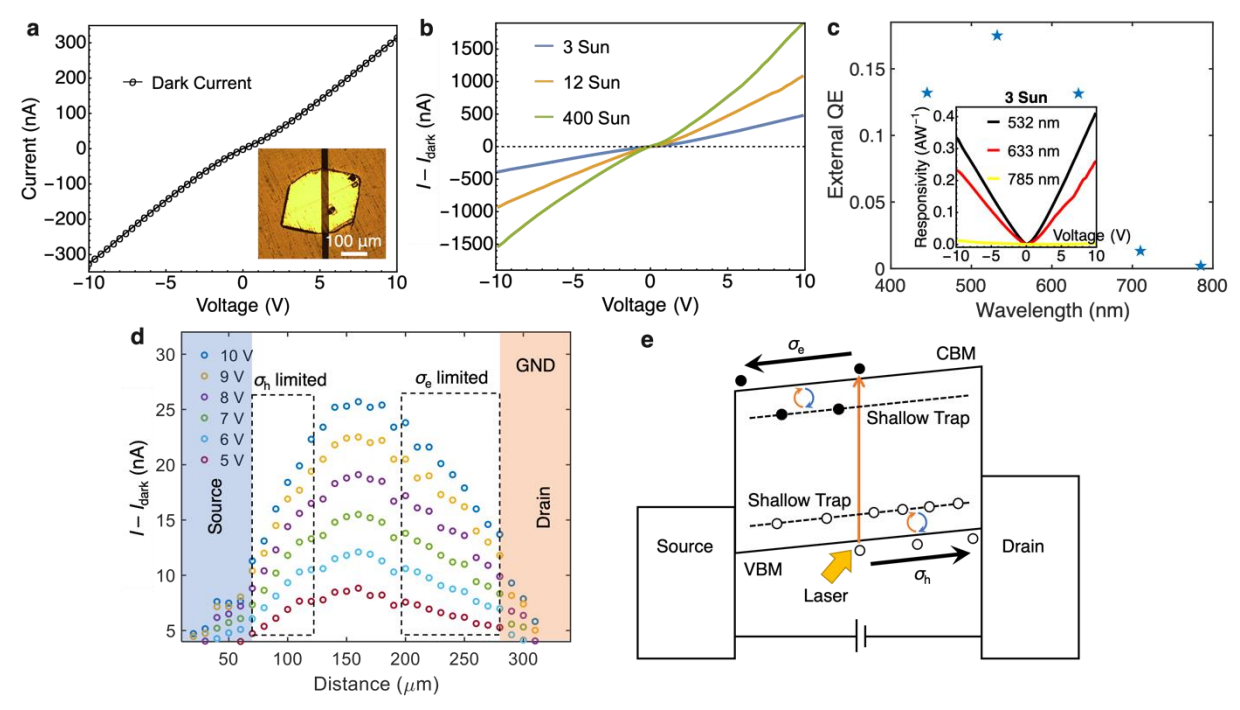
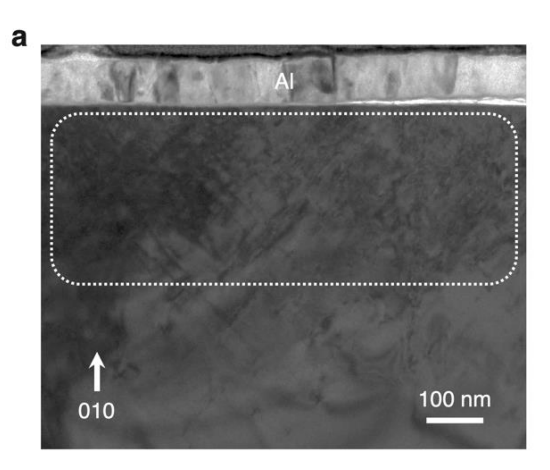


Figure 2. Photoconductivity studies on polished BaZrS₃ crystals. (a) I-V characteristics under dark conditions of a 50 μ m two terminal BaZrS₃ channel. It shows relatively linear I-V characteristics. Inset is an optical image of a 25 μ m channel with two-terminal contacts to a BaZrS₃ crystal. (b) Measured enhancement in the current upon optical illumination in the active region of the same device as (a) between the contacts. Optical illumination leads to an increase in photocurrent with increasing optical power density. (c) Wavelength dependence of responsivity or external quantum efficiency (QE) derived from the photocurrent values measured as shown in (b). (d) Spatial dependence of photocurrent across the active region of a 200 μ m two terminal BaZrS₃ channel. The maximum photocurrent value occurs when the illumination is at the center between the two contacts, irrespective of the applied bias between the contacts. This suggests BaZrS₃ turns more "conductive" by the photo-excited electrons in traps. The trap-dominated photo response is illustrated in (e) using a schematic of the band diagram. The diffusion and/or drift of electrons or holes occupying shallow traps from illuminated region to the source or drain leads to higher steady-state photoconductivity σ_e and σ_h .



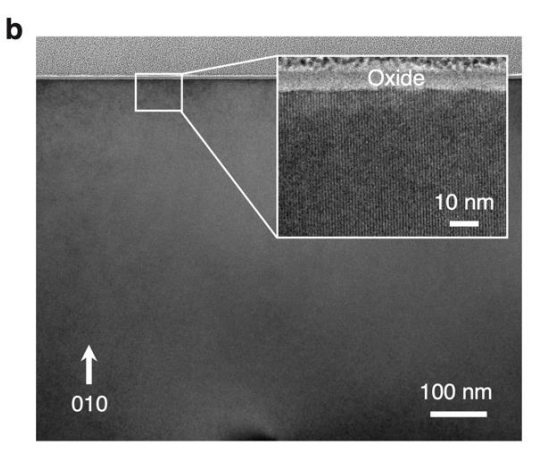


Figure 3. Extended defects introduced by mechanical polishing $BaZrS_3$. (a) STEM image of the polished $BaZrS_3$ covered by Al. Extended defects such as dislocations, stacking faults, and grain boundaries are populated down to ~300 nm into the surface, marked by a dotted box. (b) STEM image of the cleaved $BaZrS_3$ without any capping layer. No cracks or extended deformation are observed across the cleaved surface. Inset observed uniform $BaZrS_3$ (101) or (10 $\overline{1}$) atomic planes within a few nm beneath the oxide surface.

smaller than the channel length ($\sim 200~\mu m$). If one were to estimate the photo-excited carrier mean free path using the shallow decay in the spatial dependence of photocurrent, the SPCM-derived mean free path would be inconsistent with the much shorter mean free path observed in TRPL.

Hence, the decay time of the photoexcited carriers could have been extended by the traps in BaZrS₃: $\tau_{\text{decay}} = \tau_r + \tau_t (1 + \rho)^{33}$, where τ_r is the lifetime of carriers, τ_t is the time required for thermal re-excitation of trapped carriers into the conduction or valence band, ρ is the probability that an electron/hole is retrapped before recombination. Since τ_t is inversely proportional to the thermal emission rate of carriers, $\tau_t \propto \exp(-\Delta E / kT)^{34}$, where ΔE is the energy difference between the trap state and the conduction or valence band edge, accumulated trapped carriers lead to a transient photoconductive state in BaZrS₃ that rises and decays slower than photoexcited electrons and holes. The photoconductance is then dominated by the diffusion and/or

drift of trapped carriers to opposite electrodes before thermal recombine, as illustrated in Figure 2e.

Electron Microscopy Studies. To understand the origin of the discrepancy in the deduced mean free path, and whether any extended defects were created during the processing of the samples for the photoconductance studies, we carried out scanning tunneling electron microscopy (STEM) studies near the surface of a polished BaZrS₃ [Figure 3a] and a cleaved BaZrS₃ [Figure 3b]. Figure 3a shows a large number of planar defects right beneath the polished surface, which from selected area diffraction (Supporting Information) are determined to be domain walls. Considering the absorption coefficient of BaZrS₃ for 532 nm is ~2×10⁶ 1/cm⁷, most of the light is absorbed by ~ 20 nm (4x the absorption length of ~5 nm) and photo-excited carriers are largely generated within this length scale. Thus, extended defects observed here down to 300 nm would dominate the photoconductance response of the polished crystals of BaZrS₃. In

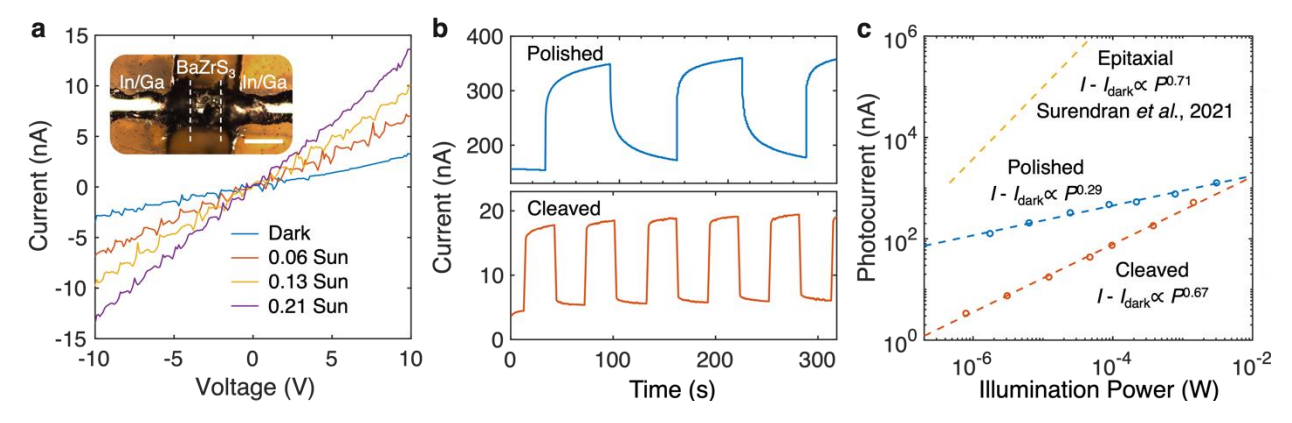


Figure 4. Photoconductance response of polished and cleaved crystals of BaZrS₃. (a) Dark and illuminated I-V characteristics of cleaved crystals of BaZrS₃. Halogen incandescent lamp with measured 0.06, 0.13, and 0.21 sun power densities were used for the measurements. Inset is the picture of two terminal junctions to a cleaved BaZrS₃, scale bar 200 μm. (b) Transient photocurrent response to 0.24 sun power white light from halogen lamp. Rise time (time to reach 90% photocurrent from dark current after illumination on): $\tau_{\text{polished}} = 18 \text{ s}$, $\tau_{\text{cleaved}} = 2 \text{ s}$; Decay time (time to reach 10% of the photocurrent after switching off excitation): $\tau_{\text{polished}} = 26 \text{ s}$, $\tau_{\text{cleaved}} = 2 \text{ s}$. Cleaved samples have a much faster photocurrent response. (c) Power law dependency of photocurrent with intensity of 532 nm illumination at +10V, fitted as $I - I_{\text{dark}} \propto P^{\theta}$. Polished BaZrS₃, $\theta = 0.29$, cleaved BaZrS₃, $\theta = 0.67$, in comparison with epitaxial BaZrS₃ (Reproduced with permission. [16] Copyright © 2021 American Chemical Society) with 10 μm channel finger geometry electrodes.

comparison, Figure 3b, STEM near a cleavage surface of Ba-ZrS₃, does not feature any noticeable cracks or other extended defects near the surface and the projection of atomic planes can be resolved within a few nm from the surface. Thus, less defective cleaved BaZrS₃ surfaces are expected to have faster photocurrent response with lower number trap states. Nevertheless, we may also note that orthorhombic²³ BaZrS₃ does not have an easy-to-cleave crystalline plane. The presumed (010) cleavage surface will be uneven during cleavage, making it non-ideal for avoiding extended defects. Thus, we anticipate that benign surface processing techniques such as chemical etching can mitigate the defect concentration that mechanical cleavage leaves in the bulk or at the surface of BaZrS₃.

Comparison of Cleaved and Polished Crystals. Next, we compare the photoconductance response of the polished and cleaved crystals by performing photoconductance studies on cleaved BaZrS3 crystals. First, the cleaved crystals of BaZrS3 show much lower dark conductance [Figure 4a] but significantly better linearity in I-V characteristics compared to the polished crystals of BaZrS3 under both dark and illuminated conditions. Moreover, Figure 4b shows the time-resolved photocurrent measurements on polished and cleaved BaZrS3 crystals, where clear differences in the time constant in the rise and decay of the photocurrent. It is evident that avoiding extended defects formed during the processing of BaZrS3 can dramatically improve the rise/decay time of the photocurrent from 18/26 s to 2/2 s; the latter is comparable to the epitaxial BaZrS₃¹⁶. Further, the contribution of the trap-contributed photo-conductance can be deduced from the power law relationship between the induced photocurrent and incident power of light, noted as I - I_{dark} $\propto P^{\theta}$, where $\theta = 1$ is the ideal photocurrent current generation and smaller θ reflects more trap-domination photocurrent generation. Figure 4c shows the relationship between photocurrent and excitation power P and the fitted powder law dependence of polished and cleaved crystals of, and epitaxial thin films of ¹⁶ BaZrS₃. It is worth noting that device geometries here are neither exactly comparable nor optimized. The power law scaling for cleaved BaZrS₃ crystals reaches $\theta = 0.67$, which is comparable to $\theta = 0.71$ of epitaxial BaZrS₃¹⁶, which is significantly higher than $\theta = 0.29$, observed for polished crystals of BaZrS₃. Thus, we show that mechanical deformation-induced extended defects play a significantly detrimental role in the optoelectronic properties of BaZrS₃.

CONCLUSION

We experimentally show that extended defects introduced by mechanical polishing are the major cause of the defect-dominated photoconductance behavior in single-crystal BaZrS₃. By avoiding such traps in cleaved BaZrS₃ crystals, the efficiency of separating photogenerated electrons and holes under DC voltage is greatly improved. Considering the relatively weak radiative recombination⁷ and photoexcited carrier mean-free-path²⁴ well over the penetration length in single crystal BaZrS₃, electrode patterning, surface passivation, electron/hole heterojunction, and defect control would further improve the optoelectronic performance of single crystals of BaZrS₃. Optimization of the contacts, surfaces, and device geometry is the next critical step for achieving high-efficiency optoelectronic and photovoltaic devices based on BaZrS₃ and other chalcogenide perovskites.

METHODS

Single Crystal Growth. BaZrS₃ crystals were grown with BaCl₂ flux. 1g of Barium Chloride powder (Alfa Aesar, 99.998%) was mixed and ground along with 0.5g stoichiometric quantities of precursor powders, including barium sulfide powders (Sigma-Aldrich 99.9%), zirconium powders (STREM, 99.5%) and sulfur pieces (Alfa Aesar 99.999%) in a nitrogenfilled glovebox. They were then loaded into a quartz tube capped with ultra-torr fittings and a quarter-turn plug valve inside to avoid exposure to the air. The tube was then evacuated to around 10 mbar and sealed.

Precursors sealed in quartz tubes were heated to 1050 °C at a ramping rate of 100 °C/h, held at 1050 °C for 100h, and then cooled to 850 °C at a cooling rate of 2 °C/h, and allowed to naturally cool down by shutting off the furnace. The obtained samples were washed with cold deionized water repeatedly for 10 min to remove the excess flux and quickly dried in desiccators. The collected crystals are then sieved into different sizes and picked out from insoluble impurities.

Time-resolved photoluminescence (TRPL). TRPL measurements were carried out with a HydraHarp400 time-correlated single photon counting system. PL was confocally excited by a 60 ps, 405 nm laser pulse at a 5 MHz repetition rate through a $50\times$ objective with a numerical aperture of 0.7. The excitation power used was~ 100μ W. The collected PL was spectrally filtered using a combination of a 630 nm long-pass filter and a 770 nm short-pass filter and detected by a pair of fast avalanche photodiodes with 16 ps time resolution.

Kelvin Probe Microscopy (KPFM). KPFM measurements were carried out using an AFM (HORIBA Scientific SmartSPM 1000) in the air. BaZrS₃ crystals cleaved or polished on the back side are connected to AFM metal specimen discs with silver epoxy. A nitrogen gun was used to remove particles on the as-grown top surface before the measurements. KPFM measurements were performed using a gold-coated Si tip with a 6 nm radius of curvature (HYDRA6R-100NG-10, APPNANO) as the probe in a noncontact mode with an AC voltage of -1 to +1 V. Crystals are illuminated under 450 nm, 532 nm, and 600 nm lasers to verify the SPV consistency.

KPFM under light illumination was carried out using XploRA Nano AFM-Raman Instrument from HORIBA Scientific. 532 nm, 638nm, and 785 nm lasers were aligned separately with the tip apex before KPFM. The XYZ coordinates of the objective were then changed by the software along with the laser selection itself in the middle of KPFM scans of polished Ba-ZrS $_3$ crystals. ND filters were changed with increments for power dependence. SPV is extracted by the ΔCPD with and without turning on the laser.

Electrical contacts to Polished Crystals. The BZS crystals were first embedded in a polymeric medium to planarize the top surface such that regular mechanical polishing and photolithography processes can be applied. The crystal planarization processing is modified from the literature³⁶ as such: BZS crystals with a thickness of ~ 100 μm or below were picked up individually by a polydimethylsiloxane (PDMS) stamp. The crystal was then embedded in a UV-curable epoxy (NOA 61, Norland Products, Inc) medium on top of a sapphire substrate (5×5 mm) by attaching the PDMS stamp adjacent to the substrate, followed by a UV curing step (*i*-line UV lamp B-100, UVP for 30 min) to solidify the epoxy. The crystal was then gently polished with a 12000-mesh polishing cloth to remove the surface oxides. Electrodes of Ti/Au (20/300 nm) were then

formed using standard photolithography and e-beam evaporation without much delay.

Electrical Connections to Cleaved Crystals. BaZrS₃ crystals were cut into half with a razor blade and loaded on Kapton double-sided tape with the cleaved surface facing up. The cleavage surface does not propagate along a specific crystalline orientation, so an uneven cleavage surface is commonly formed. Systematic electrode deposition is thus inaccessible. We then manually painted In/Ga eutectic to cover both ends of the cleaved surface to form two terminal ohmic electrical connections.

I-V Characteristics and Optoelectronic Response. I-V characterization and transient photocurrent I-t measurements were conducted using a semiconductor parameter analyzer (Agilent 4156C). Scans are carried out between DC -10V and +10V to avoid breakdown. Ambient steady-state and time-resolved photocurrent used Bausch & Lomb 20-watt halogen microscope bulb provided and controlled by Micromanipulator Probe Station to switch on or off the ambient illumination. The higher power densities were provided by solid-state lasers and attenuated by numeric apertures to control power intensity before being guided and focused on the active region of BaZrS₃.

Dark current (measured before excitation was introduced) was subtracted from light current. This gives us the unsaturated photocurrent, $I_{\rm ph} = I - I_{\rm dark}$. Incident optical power was estimated by: $P_{\rm active} = A_{\rm active} \times P_{\rm spot} / A_{\rm spot}$. Then responsivity and external quantum efficiency (EQE) at +10V DC are deducted: $R_{\lambda} = I_{\rm ph} / P_{\rm active}$, $\eta_{\rm EQE} = R_{\lambda} \times E_{\rm photon}$.

Wavelength dependence and quantitative photocurrent are achieved with 532 nm, 633 nm, and 785 nm static laser illumination provided and configured by a Renishaw Raman spectroscopy equipped with in Via confocal Raman microscope and diode lasers. 450 nm and 700 nm were performed using the Squidstat potentiostat.

Scanning Photocurrent Microscopy (SPCM). SPCM was carried out within the same Renishaw Raman spectroscopy, but the laser spot size focused to $\sim 1~\mu m$ in diameter. The scanning is achieved by a motorized stage with an accuracy of 0.1 μm across the BaZrS $_3$ terminal junction at a step of 5 μm . The finer step size is tested near the electrodes to verify consistency. Two terminal I-V characteristic is measured with a Keithley 2400 source meter under dark or illuminated conditions.

Scanning Tunneling Electron Microscopy (STEM). FIB samples were made using a Thermo Fisher Scientific Helios Dual Beam focused ion-beam. TEM samples were made from BaZrS₃ coated in Al to mitigate any charging or damage from the electron or gallium beams. Large regions of carbon and platinum were deposited with the electron beam prior to gallium beam exposure. Initial milling and cleaning steps were performed at 30 kV, which was sequentially decreased until the finishing energy of 2 kV. Aberration-corrected STEM imaging and Conventional TEM were performed on a Thermo Fisher Scientific Themis-Z STEM operating at 200 kV.

ASSOCIATED CONTENT

Supporting Information. Additional experimental details, materials, and methods, including time-resoled photoluminescence, contact geometry, kelvin probe microscopy, scanning photocurrent microscopy, and scanning tunneling electron microscopy

AUTHOR INFORMATION

Corresponding Author

* E-mail: j.ravichandran@usc.edu

Author Contributions

B.Z. and J.R. conceived the study and prepared the manuscript. B.Z., H.C., S.S., and J.R. synthesized the crystal and fabricated electrical contacts. B.Z., R.A., and R.K. carried out photocurrent studies. F.H., M.S., A.K., and J.S. performed the KPFM measurements. E.R.H. and P.E.H. executed the electron microscopy imaging and analysis.

Funding Sources

This work in part was funded by the Army Research Office (ARO) under award numbers W911NF-19-1-0137 and W911NF-21-1-0327 and by the US National Science Foundation with award number DMR-2122071. P.E.H. and E.R.H. are supported by the Office of Naval Research, Grant number N00014-23-1-2630. R.A. and R.K. are supported by the USC Provost Graduate Fellowship and National Science Foundation (NSF) under award number 2004791.

Notes

The authors declare no conflict of interest. HORIBA is the manufacturer of the AFM equipment used in this study. Collaboration with industry and academia is a part of the job responsibility for M.S. and A.K.

ACKNOWLEDGMENT

We thank Jiang Luo, Guodong Ren, and Prof. Rafael Jaramillo for the useful discussions, and Prof. Stephen B. Cronin for the support in the configurable lasers.

REFERENCES

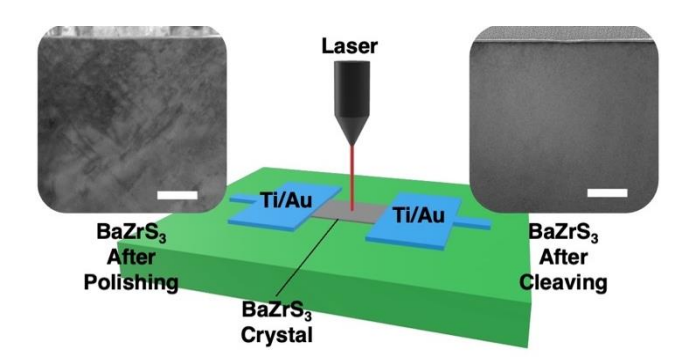
- Battaglia, C.; Cuevas, A.; De Wolf, S. High-Efficiency Crystalline Silicon Solar Cells: Status and Perspectives. *Energy Environ. Sci.* 2016, 9 (5), 1552–1576. https://doi.org/10.1039/C5EE03380B.
- (2) Kayes, B. M.; Nie, H.; Twist, R.; Spruytte, S. G.; Reinhardt, F.; Kizilyalli, I. C.; Higashi, G. S. 27.6% Conversion Efficiency, a New Record for Single-Junction Solar Cells under 1 Sun Illumination. In 2011 37th IEEE Photovoltaic Specialists Conference; IEEE: Seattle, WA, USA, 2011; pp 000004–000008. https://doi.org/10.1109/PVSC.2011.6185831.
- (3) Chen, Z.; Turedi, B.; Alsalloum, A. Y.; Yang, C.; Zheng, X.; Gereige, I.; AlSaggaf, A.; Mohammed, O. F.; Bakr, O. M. Single-Crystal MAPbI₃ Perovskite Solar Cells Exceeding 21% Power Conversion Efficiency. ACS Energy Lett. 2019, 4 (6), 1258–1259. https://doi.org/10.1021/acsenergylett.9b00847.
- (4) Saidaminov, M. I.; Adinolfi, V.; Comin, R.; Abdelhady, A. L.; Peng, W.; Dursun, I.; Yuan, M.; Hoogland, S.; Sargent, E. H.; Bakr, O. M. Planar-Integrated Single-Crystalline Perovskite Photodetectors. *Nat Commun* 2015, 6 (1), 8724. https://doi.org/10.1038/ncomms9724.
- (5) Sun, Y.-Y.; Agiorgousis, M. L.; Zhang, P.; Zhang, S. Chalcogenide Perovskites for Photovoltaics. *Nano Lett.* 2015, 15 (1), 581–585. https://doi.org/10.1021/nl504046x.
- (6) Meng, W.; Saparov, B.; Hong, F.; Wang, J.; Mitzi, D. B.; Yan, Y. Alloying and Defect Control within Chalcogenide Perovskites for Optimized Photovoltaic Application. *Chem. Mater.* 2016, 28 (3), 821–829. https://doi.org/10.1021/acs.chemmater.5b04213.
- (7) Niu, S.; Huyan, H.; Liu, Y.; Yeung, M.; Ye, K.; Blankemeier, L.; Orvis, T.; Sarkar, D.; Singh, D. J.; Kapadia, R.; Ravichandran, J. Bandgap Control via Structural and Chemical Tuning of Transition Metal Perovskite Chalcogenides. *Adv. Mater.* 2017, 29 (9), 1604733. https://doi.org/10.1002/adma.201604733.
- (8) Perera, S.; Hui, H.; Zhao, C.; Xue, H.; Sun, F.; Deng, C.; Gross, N.; Milleville, C.; Xu, X.; Watson, D. F.; Weinstein, B.; Sun, Y.-Y.; Zhang, S.; Zeng, H. Chalcogenide Perovskites – an

- Emerging Class of Ionic Semiconductors. *Nano Energy* **2016**, 22, 129–135. https://doi.org/10.1016/j.nanoen.2016.02.020.
- Hoefler, S. F.; Trimmel, G.; Rath, T. Progress on Lead-Free Metal Halide Perovskites for Photovoltaic Applications: A Review. Monatsh Chem 2017, 148 (5), 795–826. https://doi.org/10.1007/s00706-017-1933-9.
- (10) Niu, S.; Milam-Guerrero, J.; Zhou, Y.; Ye, K.; Zhao, B.; Melot, B. C.; Ravichandran, J. Thermal Stability Study of Transition Metal Perovskite Sulfides. *J. Mater. Res.* 2018, 33 (24), 4135–4143. https://doi.org/10.1557/jmr.2018.419.
- (11) Wei, X.; Hui, H.; Zhao, C.; Deng, C.; Han, M.; Yu, Z.; Sheng, A.; Roy, P.; Chen, A.; Lin, J.; Watson, D. F.; Sun, Y.-Y.; Thomay, T.; Yang, S.; Jia, Q.; Zhang, S.; Zeng, H. Realization of BaZrS₃ Chalcogenide Perovskite Thin Films for Optoelectronics. *Nano Energy* 2020, 68, 104317. https://doi.org/10.1016/j.nanoen.2019.104317.
- (12) Comparotto, C.; Davydova, A.; Ericson, T.; Riekehr, L.; Moro, M. V.; Kubart, T.; Scragg, J. Chalcogenide Perovskite BaZrS₃: Thin Film Growth by Sputtering and Rapid Thermal Processing. ACS Appl. Energy Mater. 2020, 3 (3), 2762–2770. https://doi.org/10.1021/acsaem.9b02428.
- (13) Yu, Z.; Wei, X.; Zheng, Y.; Hui, H.; Bian, M.; Dhole, S.; Seo, J.-H.; Sun, Y.-Y.; Jia, Q.; Zhang, S.; Yang, S.; Zeng, H. Chalcogenide Perovskite BaZrS₃ Thin-Film Electronic and Optoelectronic Devices by Low Temperature Processing. *Nano Energy* 2021, 85, 105959. https://doi.org/10.1016/j.nanoen.2021.105959.
- (14) Comparotto, C.; Ström, P.; Donzel-Gargand, O.; Kubart, T.; Scragg, J. J. S. Synthesis of BaZrS₃ Perovskite Thin Films at a Moderate Temperature on Conductive Substrates. *ACS Appl. Energy Mater.* **2022**, *5* (5), 6335–6343. https://doi.org/10.1021/acsaem.2c00704.
- (15) Sadeghi, I.; Ye, K.; Xu, M.; Li, Y.; LeBeau, J. M.; Jaramillo, R. Making BaZrS₃ Chalcogenide Perovskite Thin Films by Molecular Beam Epitaxy. *Adv Funct Materials* 2021, 31 (45), 2105563. https://doi.org/10.1002/adfm.202105563.
- (16) Surendran, M.; Chen, H.; Zhao, B.; Thind, A. S.; Singh, S.; Orvis, T.; Zhao, H.; Han, J.-K.; Htoon, H.; Kawasaki, M.; Mishra, R.; Ravichandran, J. Epitaxial Thin Films of a Chalcogenide Perovskite. *Chem. Mater.* 2021, 33 (18), 7457–7464. https://doi.org/10.1021/acs.chemmater.1c02202.
- (17) Turnley, J. W.; Vincent, K. C.; Pradhan, A. A.; Panicker, I.; Swope, R.; Uible, M. C.; Bart, S. C.; Agrawal, R. Solution Deposition for Chalcogenide Perovskites: A Low-Temperature Route to BaMS₃ Materials (M = Ti, Zr, Hf). *J. Am. Chem. Soc.* 2022, 144 (40), 18234–18239. https://doi.org/10.1021/jacs.2c06985.
- (18) Zilevu, D.; Parks, O. O.; Creutz, S. E. Solution-Phase Synthesis of the Chalcogenide Perovskite Barium Zirconium Sulfide as Colloidal Nanomaterials. *Chem. Commun.* 2022, 58 (75), 10512–10515. https://doi.org/10.1039/D2CC03494H.
- (19) Yang, R.; Jess, A. D.; Fai, C.; Hages, C. J. Low-Temperature, Solution-Based Synthesis of Luminescent Chalcogenide Perovskite BaZrS₃ Nanoparticles. *J. Am. Chem. Soc.* 2022, 144 (35), 15928–15931. https://doi.org/10.1021/jacs.2c06168.
- (20) Ravi, V. K.; Yu, S. H.; Rajput, P. K.; Nayak, C.; Bhattacharyya, D.; Chung, D. S.; Nag, A. Colloidal BaZrS₃ Chalcogenide Perovskite Nanocrystals for Thin Film Device Fabrication. *Nanoscale* 2021, 13 (3), 1616–1623. https://doi.org/10.1039/D0NR08078K.
- (21) Pradhan, A. A.; Uible, M. C.; Agarwal, S.; Turnley, J. W.; Khandelwal, S.; Peterson, J. M.; Blach, D. D.; Swope, R. N.; Huang, L.; Bart, S. C.; Agrawal, R. Synthesis of BaZrS₃ and BaHfS₃ Chalcogenide Perovskite Films Using Single-Phase Molecular Precursors at Moderate Temperatures. *Angew Chem Int Ed* 2023, 62 (15), e202301049. https://doi.org/10.1002/anie.202301049.

- (22) Dhole, S.; Wei, X.; Hui, H.; Roy, P.; Corey, Z.; Wang, Y.; Nie, W.; Chen, A.; Zeng, H.; Jia, Q. A Facile Aqueous Solution Route for the Growth of Chalcogenide Perovskite BaZrS₃ Films. *Photonics* 2023, 10 (4), 366. https://doi.org/10.3390/photonics10040366.
- (23) Niu, S.; Zhao, B.; Ye, K.; Bianco, E.; Zhou, J.; McConney, M. E.; Settens, C.; Haiges, R.; Jaramillo, R.; Ravichandran, J. Crystal Growth and Structural Analysis of Perovskite Chalcogenide BaZrS₃ and Ruddlesden–Popper Phase Ba₃Zr₂S₇. *J. Mater. Res.* 2019, 34 (22), 3819–3826. https://doi.org/10.1557/jmr.2019.348.
- (24) Ye, K.; Zhao, B.; Diroll, B. T.; Ravichandran, J.; Jaramillo, R. Time-Resolved Photoluminescence Studies of Perovskite Chalcogenides. *Faraday Discuss.* 2022, 239, 146–159. https://doi.org/10.1039/D2FD00047D.
- (25) Melitz, W.; Shen, J.; Kummel, A. C.; Lee, S. Kelvin Probe Force Microscopy and Its Application. Surface Science Reports 2011, 66 (1), 1–27. https://doi.org/10.1016/j.surfrep.2010.10.001.
- (26) Hansen, W. N.; Hansen, G. J. Standard Reference Surfaces for Work Function Measurements in Air. Surface Science 2001, 481 (1–3), 172–184. https://doi.org/10.1016/S0039-6028(01)01036-6.
- (27) Haynes, W. M. CRC Handbook of Chemistry and Physics, 95th Edition, 95th ed.; CRC Press: Hoboken, 2014.
- (28) Zhang, Z.; Yates, J. T. Band Bending in Semiconductors: Chemical and Physical Consequences at Surfaces and Interfaces. *Chem. Rev.* 2012, 112 (10), 5520–5551. https://doi.org/10.1021/cr3000626.
- (29) Gross, N.; Sun, Y.-Y.; Perera, S.; Hui, H.; Wei, X.; Zhang, S.; Zeng, H.; Weinstein, B. A. Stability and Band-Gap Tuning of the Chalcogenide Perovskite BaZrS₃ in Raman and Optical Investigations at High Pressures. *Phys. Rev. Applied* **2017**, *8* (4), 044014. https://doi.org/10.1103/PhysRevApplied.8.044014.
- (30) Sharma, S.; Ward, Z.; Bhimani, K.; Li, K.; Lakhnot, A.; Jain, R.; Shi, S.-F.; Terrones, H.; Koratkar, N. Bandgap Tuning in Ba-ZrS₃ Perovskite Thin Films. *ACS Appl. Electron. Mater.* 2021, 3 (8), 3306–3312. https://doi.org/10.1021/acsaelm.1c00575.
- (31) Han, Y.; Xu, J.; Liang, Y.; Chen, X.; Jia, M.; Zhang, J.; Lian, L.; Liu, Y.; Li, X.; Shi, Z. P-Type Conductive BaZrS3 Thin Film and Its Band Gap Tunning via Ruddlesden-Popper Ba3Zr2S7 and Titanium Alloying. *Chemical Engineering Journal* **2023**, 473, 145351. https://doi.org/10.1016/j.cej.2023.145351.
- (32) G03 Committee. *Tables for Reference Solar Spectral Irradiances: Direct Normal and Hemispherical on 37 Tilted Surface*; ASTM International. https://doi.org/10.1520/G0173-03R20.
- (33) Semonin, O. E.; Elbaz, G. A.; Straus, D. B.; Hull, T. D.; Paley, D. W.; Van Der Zande, A. M.; Hone, J. C.; Kymissis, I.; Kagan, C. R.; Roy, X.; Owen, J. S. Limits of Carrier Diffusion in *n* Type and *p* -Type CH₃NH₃PbI₃ Perovskite Single Crystals. *J. Phys. Chem. Lett.* **2016**, 7 (17), 3510–3518. https://doi.org/10.1021/acs.jpclett.6b01308.
- (34) Jiang, J.; Ling, C.; Xu, T.; Wang, W.; Niu, X.; Zafar, A.; Yan, Z.; Wang, X.; You, Y.; Sun, L.; Lu, J.; Wang, J.; Ni, Z. Defect Engineering for Modulating the Trap States in 2D Photoconductors. *Advanced Materials* 2018, 30 (40), 1804332. https://doi.org/10.1002/adma.201804332.
- (35) Konstantatos, G.; Levina, L.; Fischer, A.; Sargent, E. H. Engineering the Temporal Response of Photoconductive Photodetectors via Selective Introduction of Surface Trap States. *Nano Lett.* **2008**, 8 (5), 1446–1450. https://doi.org/10.1021/nl080373e.
- (36) Kang, D.; Young, J. L.; Lim, H.; Klein, W. E.; Chen, H.; Xi, Y.; Gai, B.; Deutsch, T. G.; Yoon, J. Printed Assemblies of GaAs Photoelectrodes with Decoupled Optical and Reactive Interfaces for Unassisted Solar Water Splitting. *Nat Energy* 2017, 2 (5), 17043. https://doi.org/10.1038/nenergy.2017.43.

Photoconductive Effects in Single Crystals of BaZrS₃

Boyang Zhao, Huandong Chen, Ragib Ahsan, Fei Hou, Eric R Hoglund, Shantanu Singh, Maruda Shanmugasundaram, Huan Zhao, Andrey V. Krayev, Han Htoon, Patrick E Hopkins, Jan Seidel, Rehan Kapadia, and Jayakanth Ravichandran



Photoconductive properties of single crystals of BaZrS₃ were studied. Processing-induced polishing defects lead to a transient photoconductive state, contributing greatly to the shallow-trap-controlled generation and collection of photo-excited carriers. At the same time, cleaved BaZrS₃ left fewer deformation defects and greatly improved optoelectronic properties. Defect-controlled crystal growth and contact fabrication are potentially limiting factors for achieving high photon-to-excited electron conversion efficiency in BaZrS₃.